

# **Using Automated Image Analysis for Characterization of Additive Manufacturing Powders**

Thomas F. Murphy, Christopher T. Schade, & Alex Zwiren  
Hoeganaes Corporation  
Cinnaminson, NJ

## **Abstract**

The metallic powders used as feedstock for the additive manufacturing process require evaluation of several morphological and chemical composition characteristics to ensure predictable material behavior during the manufacturing process and performance in use. The size, shape, and internal porosity of the particles are several traits requiring evaluation. Often, numerical estimates representing these characteristics are made using the digital images generated with X-ray computed tomography (CT) scans or automated image analysis (AIA). Image analysis offers several advantages over CT scans. These include lower equipment and individual test costs, higher image resolution due to higher system magnifications, and faster analysis time. In addition to the morphological analyses, particle-to-particle chemical composition uniformity is essential to maintaining the proper part microstructure. A procedure using a scanning electron microscope equipped with an energy dispersive spectrometer is described to determine the presence of particle cross-product contamination and any foreign materials.

## **Introduction**

Producing consistent parts using additive manufacturing (AM) requires knowledge of the powder feedstocks that can be helpful in predicting both the powder behavior during the build cycle and performance of the finished part. These data can be divided into two basic categories, i.e., physical or morphological and chemical characteristics. For example, the morphological properties include particle size and shape distributions, along with an estimate of the amount of gas, i.e., porosity, entrapped inside the particles. The local chemical analysis is also needed to determine the presence of particles dissimilar in chemical composition. This can be the result of contamination by another alloy powder or any foreign materials.

The most commonly used methods for examining the morphological properties are X-ray computed tomography (CT) and light optical microscopy coupled with an automated image analysis (AIA) system. Since both techniques generate and analyze images, the most accurate, reliable, and repeatable results will be a consequence of using images of the highest quality.

For the chemical analyses, the CT scans can be used for an imprecise chemical uniformity estimate, while a scanning electron microscope (SEM) equipped with an energy dispersive spectrometer (EDS) is used for more accurate measurements.

Both CT scans and AIA are vision-based systems using basically the same techniques to generate digital images for analysis. Their respective samples are illuminated by an appropriate form of energy, either high energy X-rays (CT scan) or visible light (AIA), which interacts with the sample causing changes to the intensity or appearance of the energy. This altered energy, as either attenuated X-rays or reflected light, is projected onto a flat panel detector that is sensitive to the specific energy type. Both detector surfaces are covered by a planar array of picture elements, aka, pixels, and it is the intensity or characteristics of the energy falling on the pixels that determines their digital brightness value. With the CT scans, the attenuation of the X-rays is controlled by the local sample density, while with the image analysis system, visible light reflected by the features on the metallographically prepared sample surface is captured for analysis.

Figure 1 shows a schematic of a CT scanner with the X-ray source on the left side and the energy sensitive detector on the right. The sample is located between them and rotated on an axis that allows acquisition of images at various stages during a complete revolution. The images are collected, stored, and assembled into a three dimensional representation of the sample. In many cases, the locations of the X-ray source and detector are fixed, with the position of the sample being an operator controlled variable in the system. In this design, the magnification is altered by several factors, the most important being the position of the sample in relation to the X-ray source. Moving the sample closer to the source increases the image magnification and resolution since what is projected onto the detector represents a smaller sample area. This also reduces the size of the sample that can be scanned. Formula 1 shows this relationship.

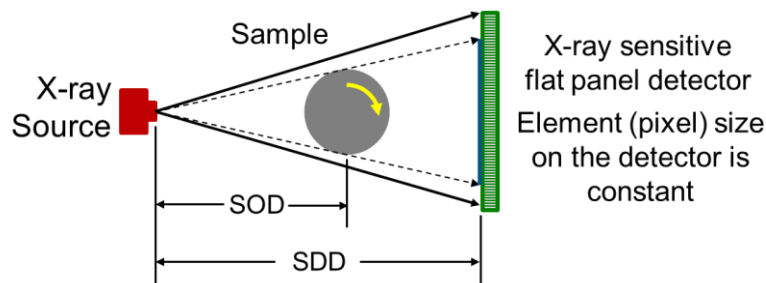


Figure 1. Schematic drawing of a CT scanner.

$$\text{Magnification} = \text{Source to Detector Distance (SDD)} / \text{Source to Object Distance (SOD)}^1 \quad (1)$$

An example of an automated image analysis system is pictured in Figure 2. It is composed of a light optical microscope (LOM) fitted with a digital camera and an automated sample stage. Where the sample is rotated in the CT scan design, the automated stage is moved in the x and y directions to collect data on

a sequence of individual fields. These data are used to characterize the morphological properties of a metallographically prepared sample. The magnification of the optical system is controlled by changing the objective lens located in the turret above the sample. As with the CT scanner, the AIA system is equipped with a computer to manage the automated operation, process images, and store data.



Figure 2. Example of a light microscope fitted with a digital camera for image capture.

While the systems share many similarities, there are distinct differences in how they are used, what they 'see' and measure, and their relative costs. Discussing all of the differences is beyond the scope of this document, but a few examples relevant to this analysis are addressed.

The biggest difference between the two techniques is that the computer-created image from the CT scan can be a 3-dimensional representation of the sample, while the AIA light microscope images are 2-dimensional. When using a CT-scanner with material images, the sample is rotated as it is illuminated by the X-ray source and two dimensional images are acquired at predetermined rotation intervals. These images are stored and assembled into a single 3-D representation of the sample using computer software designed to use image registration for accurate feature placement. With the construction of the 3-D image, volume elements, voxels, are created using the digital information from the acquired 2-D images.

Both techniques are used in a variety of disciplines, such as the life sciences, medicine, dentistry, materials science, and many others.<sup>2-5</sup> What is needed in these different analyses varies with the characteristics and details of the features of interest and their relationship to the surrounding structure. For example, if the features of interest are large, the resolution of the system can be coarse and still generate sufficient data for an acceptable analysis. In this case, a coarse or low resolution is a large linear distance represented by a single pixel in the detector array. However, the opposite is also true. In many cases, a pixel is required to represent a smaller distance where feature size is small.

Characterizing the small AM particles requires a finer, higher system resolution for the visualization and capture of the meaningful features. An additional consideration is the scale of the details defining the features. This is also affected by the same resolution conditions, where fine details require high system resolution or they will be unrecognized and ignored in the analysis.<sup>3,4,6-9</sup> Generally, the light microscopy system is able to view and define smaller features and details compared with the CT scanners due to the

ability to increase the magnification applied to the image easily. Thus, the resolution is higher as the magnification is increased.

Once the image is acquired, the features of interest must be separated or segmented from any unwanted detail. This requires well-defined boundaries between what is to be processed and measured and what is to be overlooked.<sup>3,10</sup> The combination of well-defined boundaries and a distinct variation in image contrast is necessary to make this separation. This is common to both systems and requires precisely defined images for accurate and reproducible feature separation. With the small particle size distributions used in additive manufacturing, a higher resolution image allows for more accurate segmentation of features because of the more precise definition of boundaries and edges. The segmentation process is accomplished by comparing the grayscale or color value of each pixel with a predetermined gray or color value. The pixels falling within this scale range are saved, processed, and measured, while those outside the range are neglected. With higher system resolution, there is greater accuracy in feature definition and measurement.

The types of digital images used with each analysis technique can also be different. With the CT scan, where the density of the sample determines the attenuation of the X-rays falling on the detector, the images are formed in varying shades of gray. This occurs because X-rays are not part of the visible spectrum and contain no color information. In contrast, the light used for illuminating the AIA samples is within the visible spectrum and consequently, the images analyzed may be either grayscale or color. This can be beneficial where color is an important characteristic in the microstructure. Another advantage of imaging with a light microscope is the ability to use the various light microscopy techniques, such as polarized light, darkfield illumination, differential interference contrast, etc. to provide additional information on the materials and their characteristics.

In comparing the chemical analysis capabilities of the two techniques, the CT scan is capable of determining differences in particle density, which basically shows the result of large variations in chemical composition or possibly microstructure. These are seen as changes in gray level, where more dense features appear brighter in comparison with less dense features. Making these determinations is often operator controlled and subject to inconsistent interpretation. With the SEM/EDS combination, chemical analysis can be determined on a collection of many particles or on an individual particles basis. The results can be quantitative or semi-quantitative and not subject to an operator's judgement. In these analyses, elemental dot maps were used to locate the positions of individual or multiple elements in a sample area.

### **Experimental Procedure**

Comparing the two test techniques required an understanding of the information available from each and how to make direct comparisons of these data sets. To do so, one of the first issues to be addressed was spatial resolution. The two test methods are fundamentally different in their capabilities to magnify the samples, which controls the resolution limit of the system and the amount of visible information available for processing.

A demonstration of changing image resolution can be seen in Figure 3, which was taken from a medical journal on bone analysis.<sup>3</sup> It uses CT scans on trabecular (spongy) bone from a mouse to show how the same area of a bone can appear undefined and incomplete at low resolution, improving in detail and completeness as the resolution is increased. The different voxel sizes appear under each image. As resolution is increased, details in the image are clearer, less jagged, and more complete. More information is present and a more meaningful analysis can result.

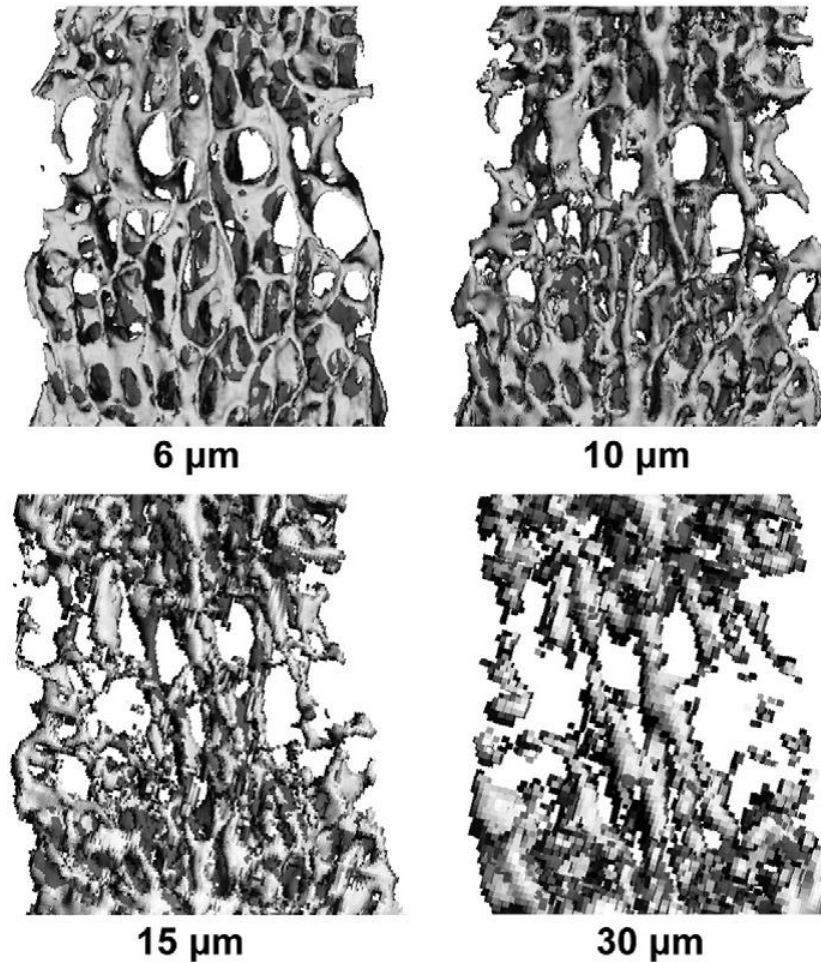


Figure 3. Effect of voxel size on the image quality and segmentation process of trabecular bone taken from a mouse. Resolution is increased with a decrease in voxel size.

A second example, a light optical microscopy sequence showing the effects of resolution on image pixelation,<sup>11</sup> is seen in Figure 4. This is a sequence of images using the same information, an image of a young starfish, at increasing resolution. In this series, the definition and color of the feature becomes clearer and better described as the resolution increases through increasing the number of pixels representing the feature. The size of the pixel array for each image is shown below each image and a rough estimate of the number of pixels used to create the image inserted into the each. In comparison with Figure 3, where areas smaller than the pixel size were missing from the bone sample, the digital representation of the colors and the details in Figure 4 are coarse and not well-defined at the lower resolutions, becoming clearer as the number of pixels is increased.

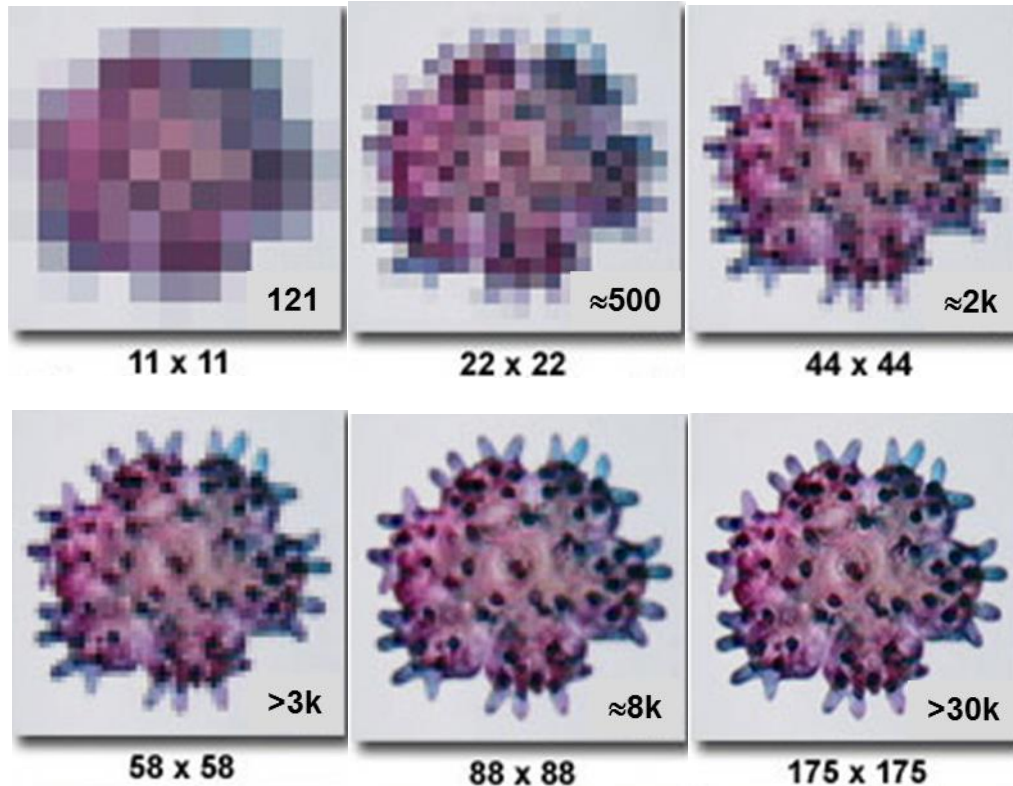


Figure 4. The effect of image resolution on the appearance of a young starfish. The number of pixels in the array used to create each image is shown below, with an estimate of the total number in each image.

Considering the examples in Figures 3 and 4, a simulation showing the visual effects of changes in pixel resolution was made using metallographically prepared metallic powder samples. This was performed on an automated image analysis system where the subject materials were powders with a typical AM size distribution. The sample compositions ranged from Ti-based alloys to stainless steel and Inconel. The intent with these simulations was to see how decreasing pixel size (increasing resolution) changed the appearance of the individual particles and what the analysis repercussions would be.

The loose powder samples were prepared using techniques described previously by Murphy.<sup>12</sup> Retaining the individual particles was of primary importance to avoid creating a size bias in the results. All samples were imaged in the unetched condition after thorough cleaning to remove any extraneous stains and dust. The same samples were also used to quantify the presence of porosity entrapped inside the particles.

After preparation, the samples were analyzed using Clemex Professional Edition automated image analysis software on light optical microscopy images provided using a Nikon Epiphot 200 inverted microscope. The image analysis procedures for the tests were routines written to have the analyses performed on an unattended, automated basis. At the conclusion of each test, the data sets were stored for later processing. With the automated nature of the process, a maximum of six samples could be analyzed in succession with a multi-sample insert for the motorized stage.

To create the simulations, digital grayscale images were captured on the AIA system and several x/y grid overlays were superimposed on them. The size of the cells in each grid was measured using the AIA

system with a 50x objective lens (0.14  $\mu\text{m}/\text{pixel}$ ), consequently each cell was composed of multiple IA pixels. The cell size within each overlay was consistent and designed to resemble the pixel size of a CT scan. Three overlays were used. The simulated pixel sizes were 6.7, 3.3, and 1.7  $\mu\text{m}$ . Figure 5 shows the appearance of the intermediate grid.

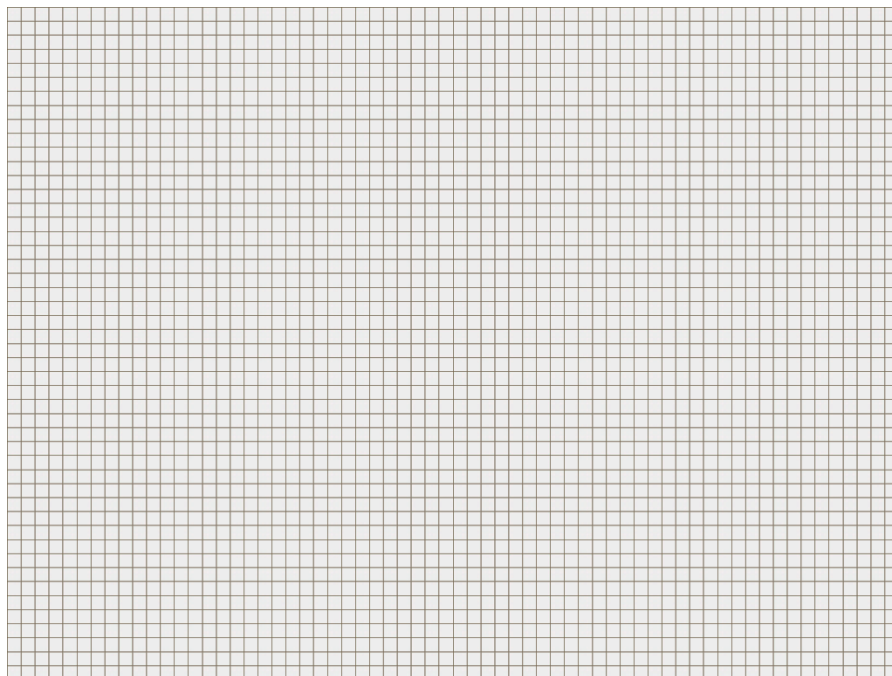


Figure 5. Full-frame image of the intermediate size overlay grid. Grid size is 3.3  $\mu\text{m}/\text{simulated pixel}$ .

Chemical analysis was performed on unpolished powder samples that had been distributed on double-sided electrically conductive adhesive tape and placed in the SEM for analysis. Using these samples, other than fixing the samples to the tape, no further preparation was needed.

A JEOL 6460 LV SEM, fitted with a Thermo Fisher Scientific System 7 X-ray microanalysis system was used for the chemical analyses. System 7 has the capability of creating the elemental dot maps used for feature comparison. Accelerating voltage was 15 keV and data acquisition times ranged from 1 to 5 minutes to create the elemental maps. Magnifications and frame resolutions were varied to investigate the relationships between particle size, pixel density, and scan time.

### **Results and Discussion**

These comparative evaluations were separated into two basic sections, morphological and chemical testing. In the morphological testing, the properties of size, shape, and internal porosity were examined. Although it is realized the particle size distribution of the powders is usually performed with laser-based systems,<sup>13,14</sup> the shape estimations rely on combinations of size measurements, i.e., lengths, perimeter, area, etc. for the estimate of shape. The chemical testing included a method to visualize particle-to-particle uniformity.

## Morphological Testing

The morphological testing requires the digital images used for evaluation to be as accurate as possible in regards to the actual shape and relative size of the particle cross-sections. As an example, Figure 6 is an image of a typical 10-45  $\mu\text{m}$  additive manufacturing powder that has been metallographically prepared and photographed using the AIA system. This light microscopy image is used in the comparison with the imaging capability of a CT scan.

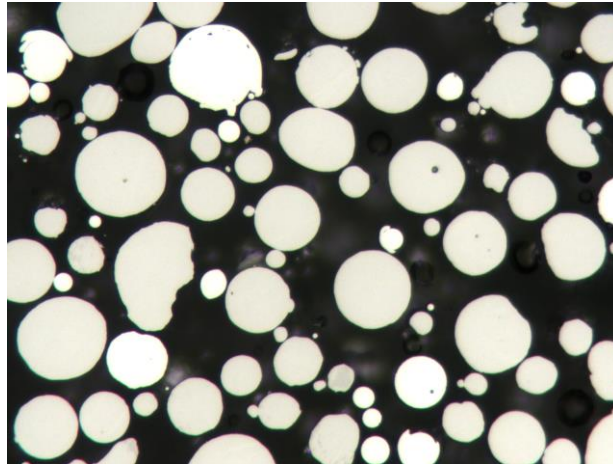


Figure 6. Cross-sectional image of a Ti6Al4V additive manufacturing powder. The resolution of this image is 0.14  $\mu\text{m}/\text{pixel}$ .

In Figure 7, the simulated pixel sizes of 6.7, 3.3 and 1.7  $\mu\text{m}/\text{pixel}$  are overlaid onto the LOM image from Figure 6. The orange portions of the figures are what would be used to represent the individual particles at the different simulated pixel sizes. These are complete cells, while the blue areas at the particle edges are partial cells. In Figures 7b, d, and f, the complete squares are the visible representations of the particle cross-sections. At the largest cell size, multiple smaller particles are not recognized and consequently, shown without overlaid orange cells. These illustrations are analogous to the bone images in Figure 3, where sections are missing at larger voxel sizes and the surfaces are unacceptably jagged. The blue edges in Figures 7a, c, and e are the partial cells, which remain ignored in the detection process unless special computer manipulation of the data is used to include them.

Detected Simulated Pixels, Complete and Partial

Completely Contained Simulated Pixels

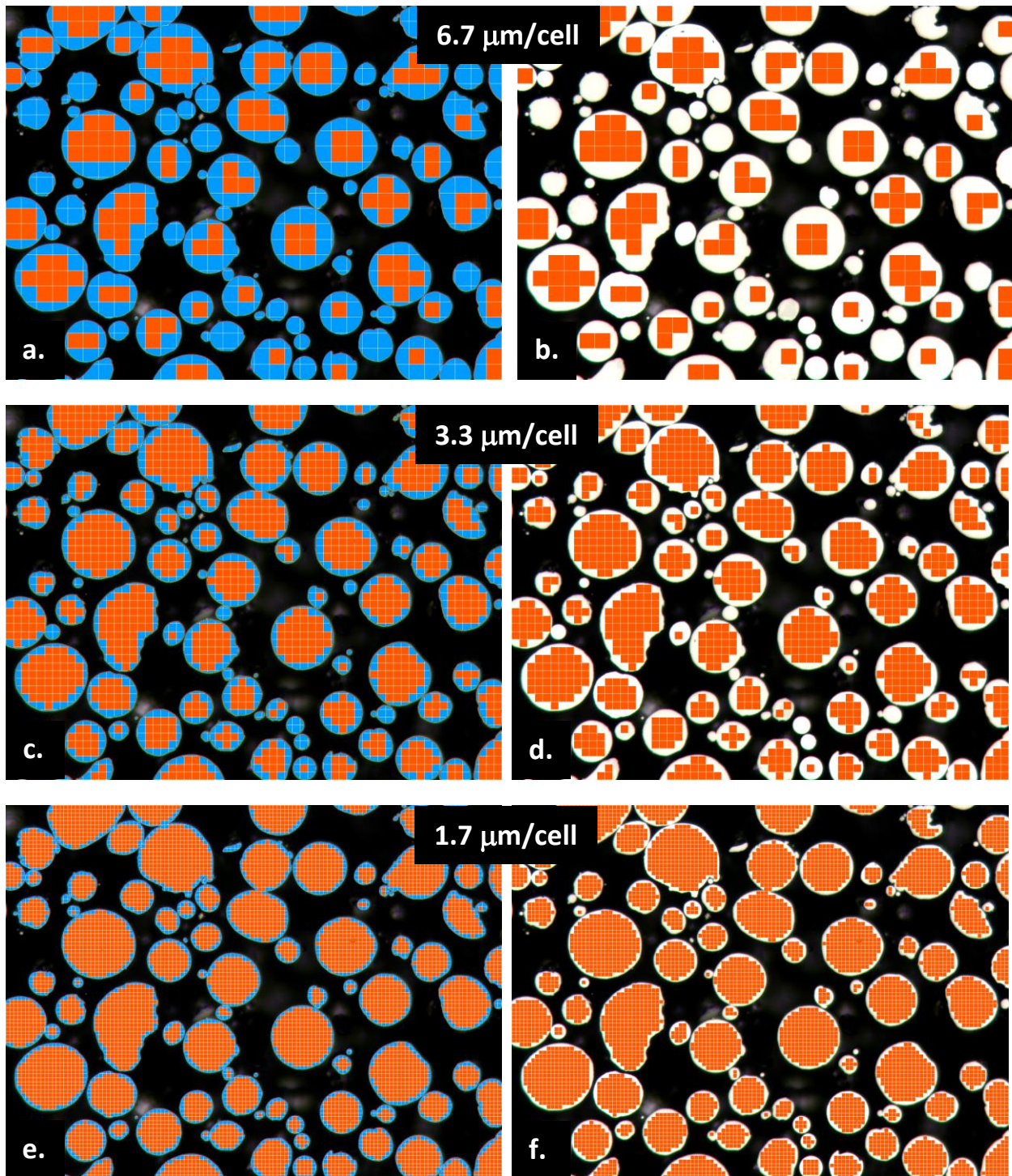


Figure 7. Visualization of the particles using the three simulated pixel size grid overlays.

Additionally, it should be recognized that the number and placement of the overlaid cells is affected by the coincidence of the detector elements with the particles. With the detector constructed as an ordered

x/y array of pixels and the particles randomly distributed throughout the analysis area, the number of the pixels defining each particle is unlikely to be maximized due to their superimposed locations.

The blue particle edges in Figure 7a, c, and e contain varying amounts of both the particle cross-sections and mounting material. This is the boundary between the portion of the image to be used in the analysis and what will be ignored. An enlarged illustration can be seen in Figure 8. This is an area from another processed image with the continuous white areas being the particle definitions at the three simulated pixel overlays. The blue squares are the locations where pixels consist of the two components. The curved lines inside the blue cells show the locations of the particle perimeters and the amount of white and black, particle and mounting material, can be estimated by the position of the perimeter inside the blue square. Consequently, the digital gray value of these pixels varies with the proportions of the highly reflective and less reflecting components in the microstructure. This condition affects not only feature recognition but also segmentation of the features of interest from the remainder of the microstructure. It is also present with the three dimensional imaging techniques, such as CT scans, where it is referred to as the Partial Volume Effect (PVE).<sup>5,10,15,16</sup> Computer software has been developed to use these proportions of wanted and unwanted feature information, attempting to make the characterizations more accurate. The downside to this image manipulation can be the introduction of extraneous information and noise into the image, which can be mistaken for feature data and included in the analysis.

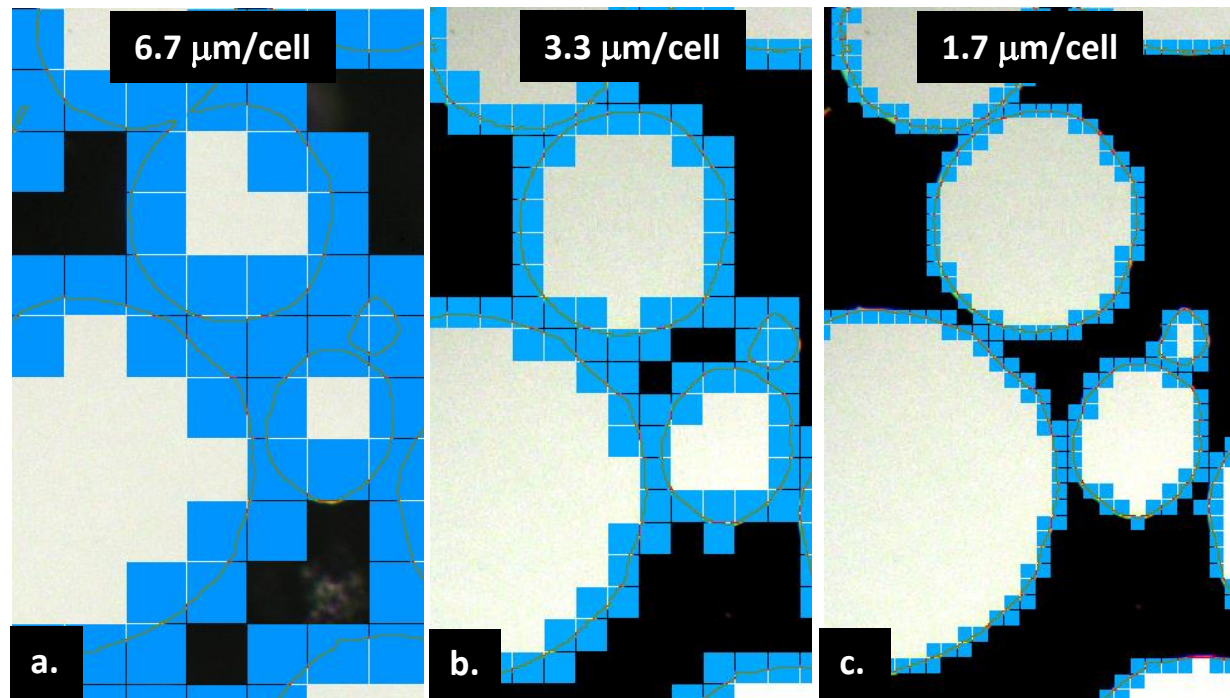


Figure 8. Enlarged area of a processed image containing the three sizes of simulated pixels at particle edges in addition to the particle perimeters.

While the previous figures used a simulation of different pixel sizes to show how the processed image appearance is affected by them, Figure 9 is an image of a 10-45 μm gas atomized additive manufacturing powder imaged using a commercially available CT scanner. The pixel-voxel size used for this imaging was 3.5 μm/pixel, the highest resolution available with this scanner. Size and shape details of the

individual particles are difficult to determine due to the lack of feature definition. It should be noted the finest simulated pixel example in Figure 7 is twice the resolution of CT scan used to acquire the image and data from Figure 9.

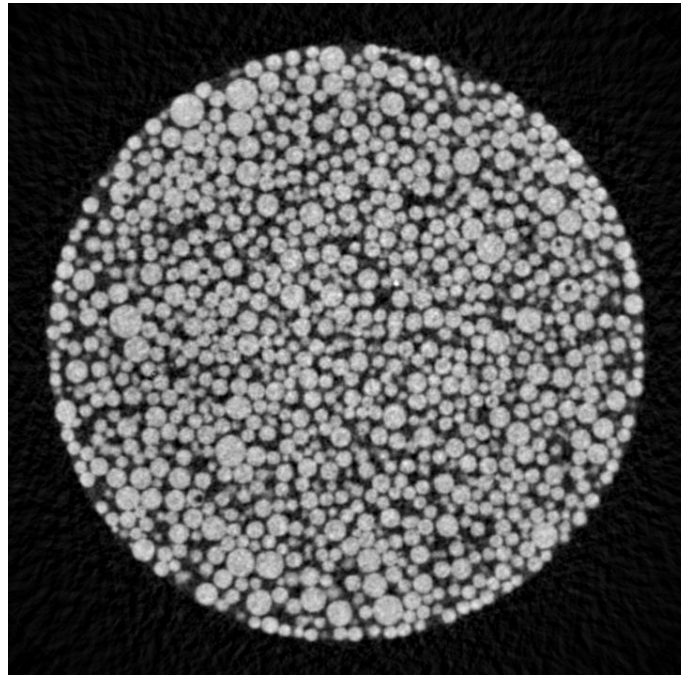


Figure 9. CT scan section of a gas atomized additive manufacturing powder at a resolution of  $3.5 \mu\text{m}/\text{pixel}$ .

In comparison with the CT scan information, Figure 10 uses images from the LOM-AIA combination at several levels of magnification to illustrate how the pixel size and ability to change magnification help in defining the features. In each photomicrograph, the pixel size remains the same, but the size of the features in the image changes with increases in magnification. Consequently, each feature is characterized by more pixels with increases in magnification and more detail, especially at the edges, is defined.

The left images, Figure 10a, c, and e, show entire fields at three resolutions. The right images, b, d, and f, are the segments of the whole field images outlined with a red rectangle and subsequently enlarged 8 times to show the pixel size. While changing the magnification introduces a requirement that more fields be examined to see the same number of particles (4 times the fields for a doubling of the magnification) the amount and quality of information available is improved to show more detail. This is especially apparent at the feature edges where interparticle friction is important in particle behavior during part build. Increasing the magnification, with the resulting increase in resolution, also uses more pixels to define each particle, making the pixels at the feature edges less meaningful to the overall evaluation.

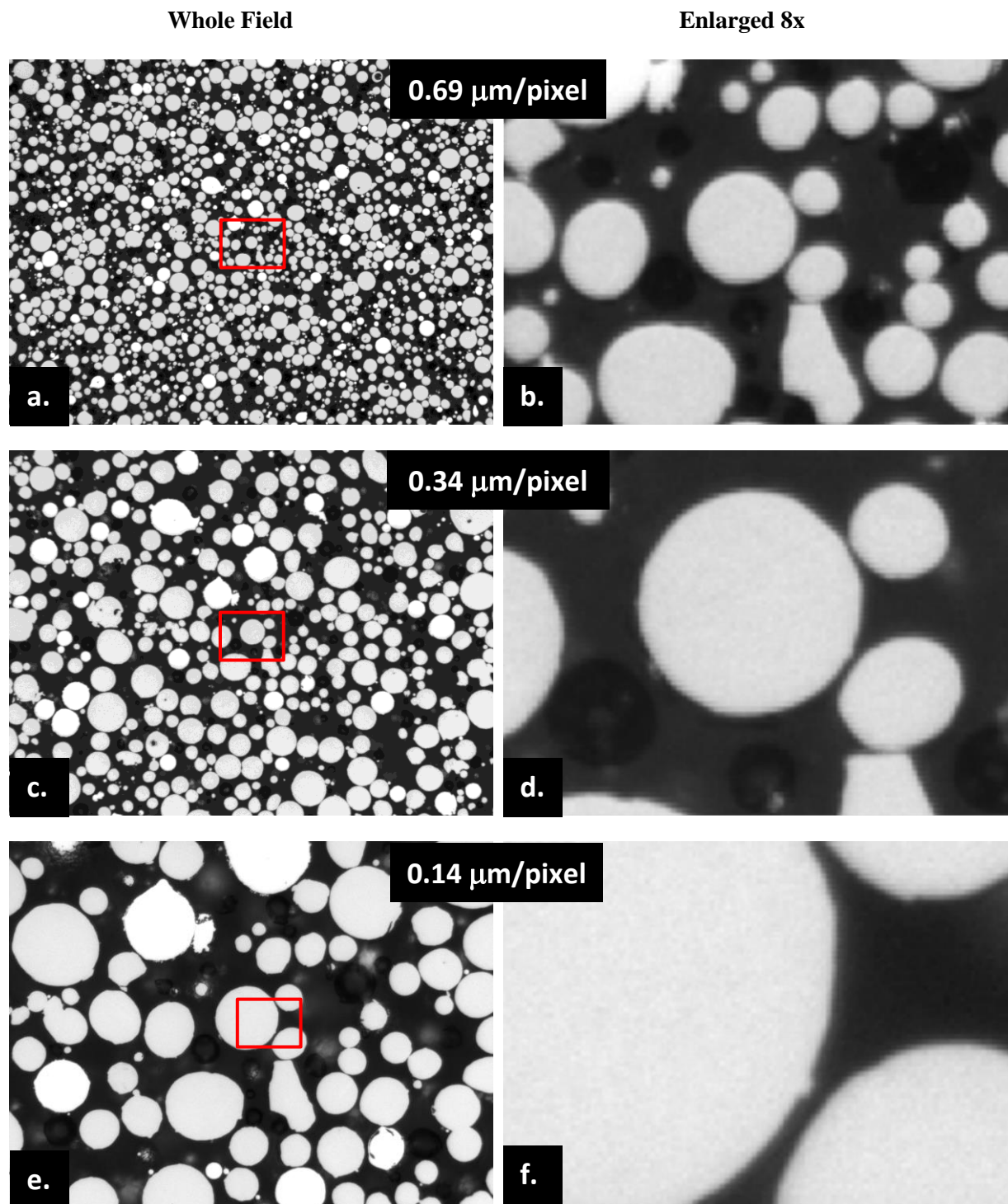


Figure 10. Light optical microscopy images acquired using the automated image analysis system. The left images are whole fields, while the right images are the regions within the red rectangles enlarged 8 times. Although difficult to see, the actual square representation of the pixel size is visible in b, d, and f.

Once the image is digitized, the process of separating the areas of interest from the entire field must be accomplished accurately for the subsequent processing and measurements to be as close to the original as

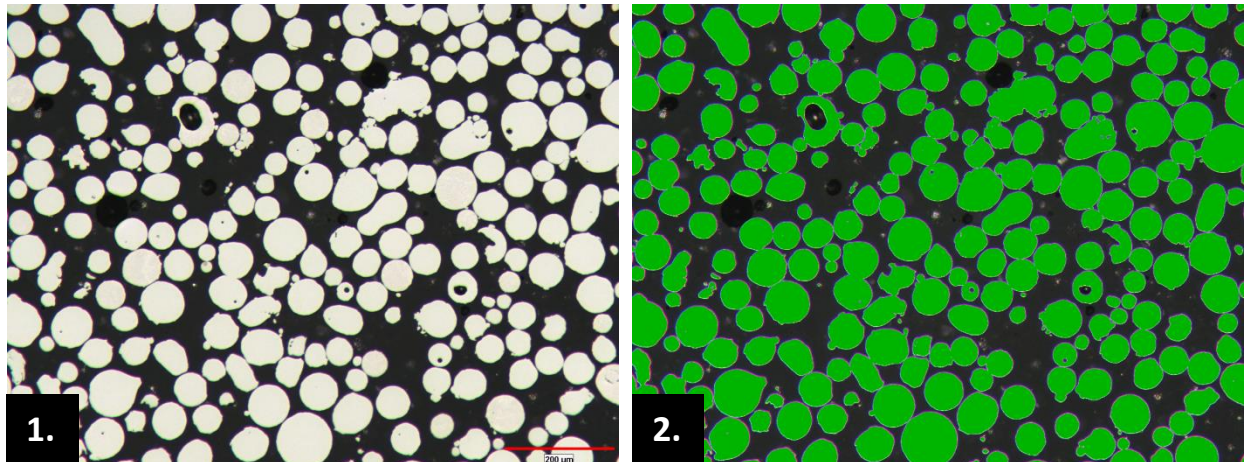
possible. This is done by comparing the digital graylevel or color value of each pixel with a predetermined gray or color range and separating all pixels falling within this range from those outside. With higher resolution, the ability to make this segmentation is more accurate in defining the individual features. Depending on the system, both AIA and CT scanners have automated or manual methods for this process. Sometimes, it is details in the sample that dictate the segmentation method. After storage of the wanted information, all image processing and measurement can be made.

With AIA, the size measurements include several lengths, perimeter, and area. It is from these data that the shape is estimated. Currently, the expression in Formula 2 is used to compare particle shapes. This uses the shape of a circle as the maximum value, which is 1. Any shape more irregular than that of a circle will have a value of <1. Many other possibilities exist and can be implemented when needed.<sup>12,17,18</sup>

$$4\pi A/P^2 \quad (2)$$

where A is the section area and P is the perimeter.

The AIA sequence of quantifying porosity within the particles can be seen in the series of photomicrographs in Figure 11. They demonstrate the sequence of image processing and how the separation of pores from the particle cross-sections can be made. In order of processing, step 1 is acquisition of the grayscale image, followed by comparing the grayscale range of the pixels with a predetermined grayscale, with those falling within the grayscale shown as green (step 2). Next in step 3, detected particles touching other particles from the mounting operation are separated, with locations of created boundaries with the small yellow circles. If required, the algorithm used for this separation can be adjusted to fit the amount of contact. The pore locations within the particles are located in step 4 and finally, the pores in red are shown for measurement in step 5. This powder is gas atomized and shown at a resolution of 0.34  $\mu\text{m}/\text{pixel}$ .



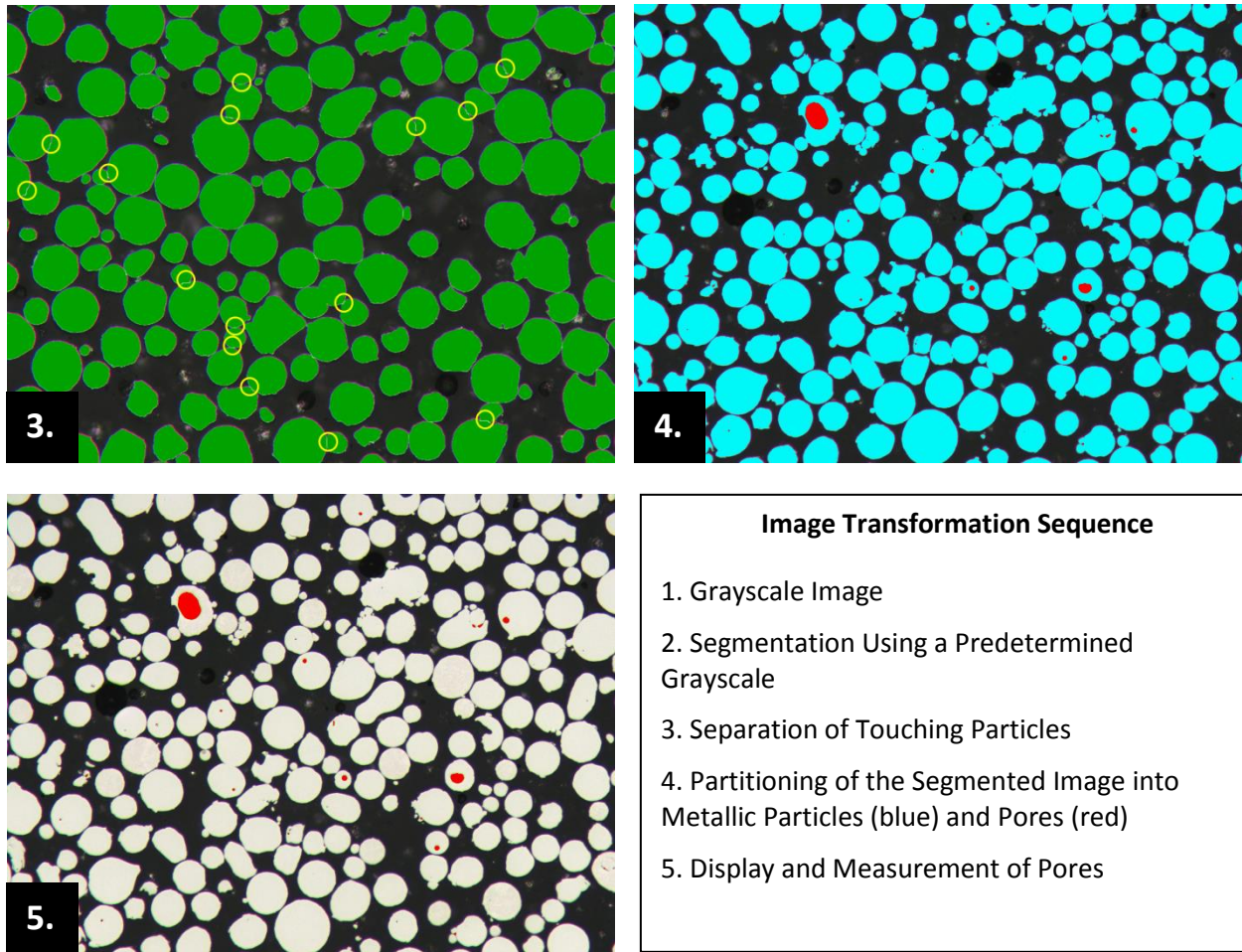


Figure 11. Image processing sequence for the analysis of porosity entrapped inside particles.

With the pore analysis, multiple measurements and calculations are made. They include the area percent porosity contained in the total metallic area fraction, the percentage of the particles containing pores, the pore size distribution, and others where needed. It has also been shown that 2-dimensional AIA estimates of the porosity content in AM materials compared well with 3-dimensional estimates from CT scanning.<sup>19-22</sup>

In regards to the testing time, it is difficult to estimate the CT time required to analyze a sample since generation of the images, operator interaction, and data manipulation must all be included in the times and these vary with the equipment, personnel, and desired outcome. With the AIA system, once the test method is developed, sample preparation requires 1-1½ hours and the analysis time is usually <10 min/sample. Specifically, analysis of between 20,000 and 50,000 particles was accomplished in <7 minutes in this research/method development program. The variability in the number of measured particles was due to the particle size distribution of the alloys. At the conclusion of testing, averages and distribution values are generated by the AIA system and the individual feature data is stored if further manipulation is needed.

## Chemical Analysis

Chemical analysis is performed on additive manufacturing powders to assure the particle-to-particle uniformity in the powder mass. Variation in local alloy content may result in differences in microstructure, which could cause problems in part performance. In production facilities where multiple alloys are used, the possibility exists that one alloy could accidentally contaminate another, aka, cross-product contamination. In addition, powder transportation and handling could cause introduction of foreign materials. In both cases, accurate and reliable methods are needed to determine the presence of contamination particles and if possible, identify them.

CT scans are sometimes used for these tests, however, because the scanner relies on variations in density to determine alloy composition differences, the density difference must be fairly substantial to give a clear indication of the contamination. Historically, some of the original testing performed on titanium alloys in additive manufacturing was concentrated on detecting the presence of tungsten particles. This is relatively simple since the density of a Ti-6Al-4V is approximately  $4.4 \text{ g/cm}^3$  while tungsten is approximately  $19.3 \text{ g/cm}^3$ . In this case, the W particles will appear as bright particles in a mass of darker, lower density features. Unfortunately, no information on chemical composition is generated.

Although large differences in density, such as the one mentioned above, are easily analyzed, problems arise when the compositions of possible contaminants are closer in density, such as stainless steel, Ni-base alloys, or even a mixture of two Ti alloys. In these cases, the CT scan would possibly be unable to distinguish one material from another.

In order to find an improved chemical testing method, a scanning electron microscope equipped with an energy dispersive spectrometer was used to perform tests on several powders into which contaminants were intentionally added. The goals of the testing were to locate any contaminants that were present, determine their chemical composition, and find ways of displaying their presence that would be easily understandable and not subject to operator interpretation.

Initially, an SEM imaging technique using backscattered electron images (BEI) was used to imitate the effect of density used by the CT scan. These images are formed in the SEM based on atomic number differences, where higher atomic number features appear brighter than those of lower atomic number. In looking again at the comparison of Ti and W, where the densities were vastly different for CT scan imaging, their atomic numbers are 22 for Ti and 74 for W. Again, this would not present a problem to determine a difference between these two elements using an imaging technique, nor would alloys containing a base of these elements be difficult.

A viability test was designed for this contamination study using a Ti-6Al-4V powder as the base. This was doped with varying amounts of 316L stainless steel and Inconel 625 additive manufacturing powders with the same basic shape distribution, however the 316L had a finer size distribution. The approximate percentages for doping were 0.5 wt/o 316L and 5 wt/o Inconel 625. BEI were acquired on both samples and maps using the locations of the major alloying elements were made for each example. Sample preparation of the powders was simply to fix the loose powders to a double-sided electrically conductive adhesive tape. It was also found that using particle cross-sections in metallographic mounts was possible, although the samples would probably require coating with an electrically conductive material, most likely carbon.

Figure 12 shows the results of the Inconel 625 contamination. In this case, the particular colors in the elemental map were chosen to represent the elements in both the base and contaminant that would present a distinction between the two alloys. With the BEI, a contrast difference is seen between the heavier Ni-base Inconel and the Ti alloy. The monochrome backscattered electron image shows multiple particles slightly brighter compared with the background. In the elemental map image, the blue Ti alloy is well contrasted with the yellow Inconel particles. The yellow particles in the elemental map correspond to the brighter particles in the BEI image.

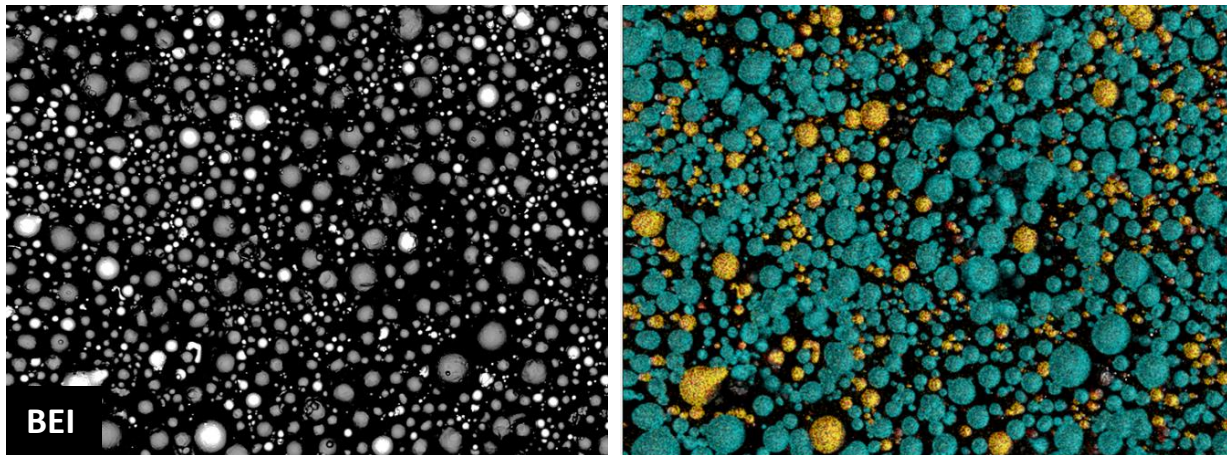


Figure 12. BEI of the particle distribution (left). Right image is an elemental map showing the presence of the Inconel 625 contaminant (yellow) in the Ti-6Al-4V base (blue).

The same comparison set of images was made with the sample contaminated with the 316L stainless steel. Images similar to those in Figure 12, are used with the contaminated Ti alloy in Figure 13. A similar blue color is again used to represent Ti and the small stainless steel particles imaged in red. The BEI was not as clear in separating the two alloys as with the Inconel. This could be because the contaminant powders were considerably smaller in particle size distribution.

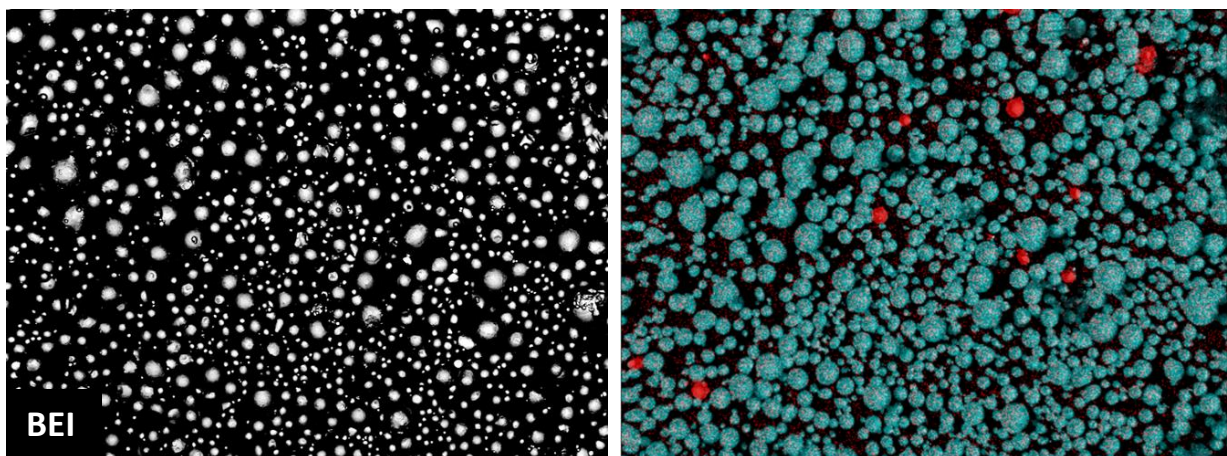


Figure 13. BEI of the particle distribution (left). Right image is an elemental map showing the presence of the 316L contaminant (red) in the Ti-6Al-4V base (blue).

To show further effectiveness of the test method, a blind test was performed using the same Ti-6Al-4V base alloy, but with the contaminants as two other Ti alloys. The two alloys chosen were a Beta 21S (Ti+15Mo+2.8Nb+3Al) and a commercially pure titanium (CP Ti Grade 1 or 2). The CP Ti is basically Ti with  $\leq 0.3$  Fe and  $< 0.25$  O. The approximate amounts of the added contaminants was 3 wt/o of the CP Ti and 1 wt/o Beta 21S. These samples were imaged using secondary electrons (SEI) since the atomic number difference in the base and added alloys was not sufficient to show a clear contrast difference.

Figure 14 is the combination of particles with CP Ti used as the dopant. In this case, the base Ti-6Al-4V particles are a yellowish color while the CP Ti are red. The Beta 21S results are shown in Figure 15, where the Ti-base alloy is an orange color and the contaminant is yellow.

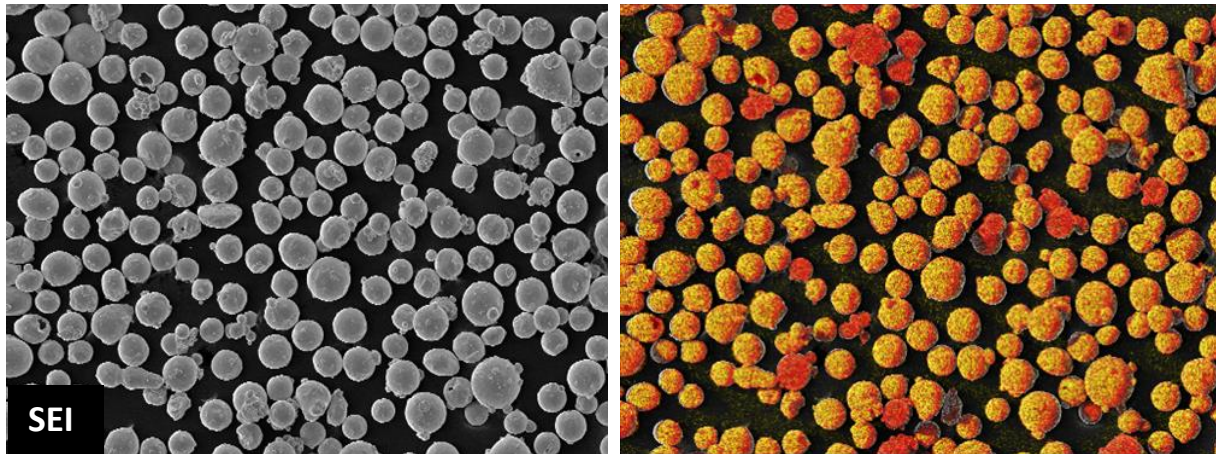


Figure 14. SEI of the Ti-6Al-4V with added CP Ti. The right image is the elemental map showing locations of particles of each composition – Ti-6Al-4V yellow, CP Ti red.

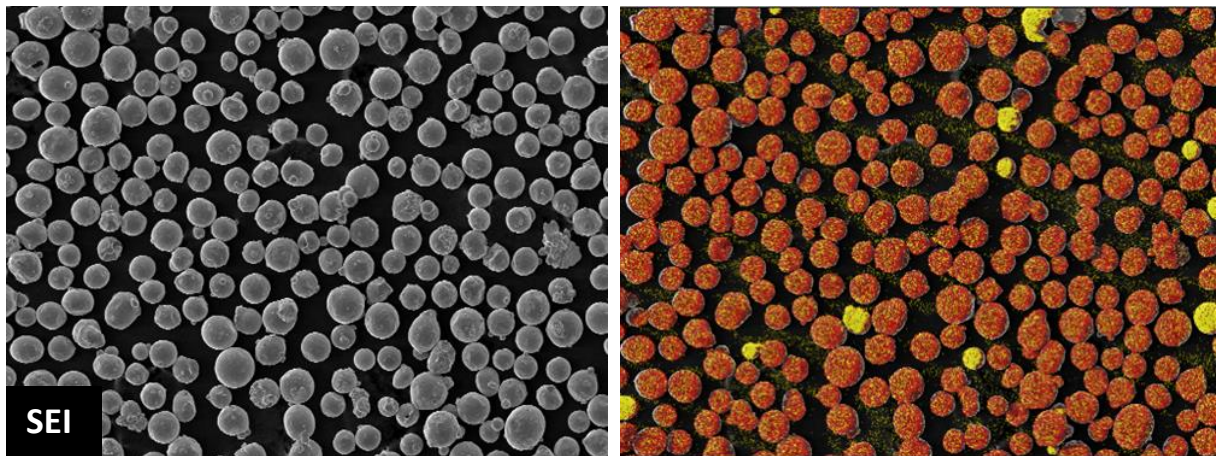


Figure 15. SEI of the Ti-6Al-4V with added Beta 21S. The right image is the elemental map showing the locations of particles of each composition. Ti-6Al-4V orange, Beta 21S yellow.

With these tests, it was found the magnifications could be varied to control the number of particles imaged and what is used in this document seems to be a good compromise between defining the contaminants and showing a reasonable number of particles in one field. When making the elemental

maps, knowledge of the EDS operation is essential in determining a good combination of elements to be mapped and how to combine the colors to distinguish one alloy from another. Colors can be chosen as complimentary colors or to reinforce the color of multiple elements. When dissimilar particles are found, the magnification can be increased and an analysis performed on the single particle if desired. The results can be qualitative, semi-quantitative, or quantitative with the use of standards.

### **Cost Comparison**

Equipment costs for a CT scanner and an automated image analysis system can be vastly different, with system capabilities determining much of the cost. An AIA system, including an optical microscope, automation, camera, etc. can be purchased for as little as \$50,000. However, this price could increase to double or more depending on the microscope and digital camera. In comparison, a CT scanner with the ability to perform the tests described in this paper will be most likely be 10x the AIA price or higher for a microCT scanner.

Purchasing a SEM with an EDS system to perform chemical analysis on the individual particles will be in the neighborhood of \$100,000, but can escalate to several times that price depending on the configuration and capabilities of the microscope. An additional benefit of this microscope is the potential to image the powder particles at magnifications considerably higher than what is possible using a LOM or CT scanner and examine them in greater detail, acquiring more information.

### **Conclusions**

The combination of automated image analysis and scanning electron microscopy offer several advantages over computed tomography testing for the analysis of metallic powders used in additive manufacturing. These include:

- Increased imaging resolution to  $\ll 1 \mu\text{m}/\text{pixel}$  and the attendant ability to provide more visible detail and information on the small additive manufacturing powders.
- Measurement of size using a variety of linear and areal measurements, in addition to combining these measurements into relationships where particle shape can be estimated.
- Detection and measurement of the porosity contained within the individual particles and the determination of percentage pore volume, the percentage of the particles containing pores, and others.
- Determination of chemical analysis uniformity on an individual particle basis through energy dispersive X-ray analysis. This can be detection of foreign material or contamination of a base alloy with another dissimilar in composition.
- A possible reduction in equipment cost and the time to perform the testing.

### **References**

1. J.J. Lifton, A.A. Malcom, J.W. McBride, and K.J. Cross, "The Application of Voxel Size Correction in X-ray Computed Tomography for Dimensional Metrology", Singapore International NDT Conference and Exhibition, 2013, pp. 1-11.

2. A. du Plessis, S.G. le Roux, and A. Guelpa, "Comparison of Medical and Industrial X-ray Computed Tomography for Non-Destructive Testing", *Case Studies in Nondestructive Testing and Evaluation*, 2016, pp. 17-25.
3. B.A. Christiansen, "Effect of Micro-Computed Tomography Voxel Size and Segmentation Method on Trabecular Bone Microstructure Measured in Mice", *Bone Reports*, 2016, vol. 5, pp. 136-140.
4. Y.-H. Sang, H.-C. Hu, S.-H. Lu, Y.-W. Wu, W.-R. Li, Z.-H. Tsang, "Accuracy Assessment of Three-Dimensional Surface Reconstructions of *In Vivo* Teeth From Cone-beam Computed Tomography", *Chinese Medical Journal*, 2016, vol. 129, no. 12, pp. 1464-1470.
5. J. Tohka, "Partial Volume Effect Modeling for Segmentation and Tissue Classification of Brain Magnetic Resonance Images: A Review", *World J. Radiol.*, 2014, vol. 6, no. 11, pp. 855-864.
6. J. Rueckel, M. Stockmar, F. Pfeiffer, and J. Herzen, "Spatial Resolution Characterization of a X-ray MicroCT System", *Appl. Radiat. Isotopes*, 2014, vol. 94, pp. 230-234.
7. "Resolution and Size Limitations", U. Texas Geosciences, <http://www.ctlab.geo.utexas.edu/about-ct/resolution-and-size-limitations/>
8. L.W. Goldman, "Principles of CT: Radiation Dose and Image Quality", 2007, *J. Nucl. Med. Technol.*, 2007, vol. 35, no. 4, pp. 213-225.
9. D. Maret, N. Telmon, O.A. Peters, B. Lepage, J. Treil, J.M. Inglese, A. Peyre, J.L. Kahn, and M. Sixou, "Effect of Voxel Size on the Accuracy of 3D Reconstructions with Cone Beam CT", 2012, *Dentomaxillofacial Radiology*, vol. 41, pp. 649-655.
10. T.W. Way, H-P. Chan, B. Sahiner, M.M. Goodsitt, L.M. Hadjiiski, C. Zhou, and A. Chughtai, "Effect of CT Scanning Parameters of Volumetric Measurements of Pulmonary Nodules by 3D Active Contour Segmentation: A Phantom Study", *Phys. Med. Biol.*, 2008, vol. 53, no. 5, pp. 1295-1312.
11. K.R. Spring, J.C. Russ, and M.W. Davidson, "Basic Properties of Digital Images", 2012, <http://www.olympusmicro.com/primer/digitalimaging/digitalimagebasics.html>
12. T.F. Murphy, "Metallographic Testing of Powders Intended for Use in Additive Manufacturing", *Int. J. Powder Metall.*, 2016, vol. 52, no. 1, pp. 25-35.
13. "Particle Size and Shape Measurement Using Image Analysis", Malvern Instruments, [http://surfaceanalysis.ru/surface/categories/1f/74/content\\_128015234686.pdf](http://surfaceanalysis.ru/surface/categories/1f/74/content_128015234686.pdf)
14. "A Guidebook to Particle Size Analysis", 2016, Horiba Instruments, Inc., Irvine, CA.
15. M. Soret, S.L. Bucharach, and I. Buvat, "Partial-Volume Effect in PET Tumor Imaging", *J. Nucl. Med.*, 2007, vol. 48, no. 6, pp. 932-945.
16. "Artifacts and Partial-Volume Effects", U. Texas Geosciences, <http://www.ctlab.geo.utexas.edu/about-ct/artifacts-and-partial-volume-effects/>
17. D.W. Hetzner, "Comparing Binary Image Analysis Measurements – Euclidean Geometry, Centroids and Corners", *Microscopy Today*, 2008, vol. 16, no. 4, pp. 10-15.
18. J.M. Rodriguez, T. Edeskar, and S. Knutsson, "Particle Shape Quantities and Measurement Techniques – A Review", *Elect. J. Geotechnical Eng.*, 2013, vol. 18/A, pp. 169-198. <http://www.ejge.com/2013/Ppr2013.016alr.pdf>
19. K. Heim, F. Bernier, R. Pelletier, and L.-P. Lefebvre, "High Resolution Pore Size Analysis in Metallic Powders by X-ray Tomography", *Case Studies in Nondestructive Testing and Evaluation*, 2016, vol. 6, pp. 45-52.

20. F. Bernier, R. Pelletier, L.-P. Lefebvre, and K. Heim, "Powder Characterization Using X-ray Tomography and Image Analysis", *Advances in Powder Metallurgy & Particulate Materials-2016*, compiled by C. Blais & J. Hamilton, Metal Powder Industries Federation, Princeton, NJ, 2016, part 11, pp. 726-735.
21. F. Leonard, S. Tammam-Williams, and I. Todd, "CT for Additive Manufacturing Process Characterisation: Assessment of Melt Strategies on Defect Population", 2016, *6<sup>th</sup> Conference on Industrial Computed Tomography*, Wels, Austria (iCT 2016), pp. 1-8.
22. A. Singhal, J.C. Grande, and Y. Zhou, "Micro/Nano-CT for Visualization of Internal Structures", *Microscopy Today*, 2013, vol. 21, no. 2, pp. 16-22.